


# Landé $g$ Factor of Excitons from Circularly Polarized Low-Field Magnetomodulated Reflectance Spectroscopy: Application to Bulk $2H$ -MoS<sub>2</sub>

Dibyasankar Das<sup>1</sup>, Vishwas Jindal<sup>1</sup>, Vasam Sugunakar, and Sandip Ghosh<sup>1\*</sup>

*Department of Condensed Matter Physics and Materials Science, Tata Institute of Fundamental Research, Mumbai 400005, India*

 (Received 4 January 2023; revised 1 May 2023; accepted 30 May 2023; published 26 June 2023)

Measurement of the Landé  $g$  factor (LGF) normally involves determining the energy splitting of spectral features under a dc magnetic field of several teslas. We show that circular-polarization-resolved magnetomodulation spectroscopy, with a small ac field of the order of 50 mT rms, can be used to measure the LGF of excitons in semiconductors. The technique is easy to implement with a microscope arrangement, enabling measurements with high spatial resolution at cryogenic temperatures. We validate the technique and determine its limits through measurements on excitons in a GaAs/Al<sub>0.3</sub>Ga<sub>0.7</sub>As quantum well. We then apply it to microscopic flakes of bulk  $2H$ -MoS<sub>2</sub> and determine the LGF of the ground-state  $A_{1s}$  exciton and the next-higher-energy exciton labeled  $IL$ , at energies around the direct gap of  $2H$ -MoS<sub>2</sub>. The LGF of  $IL$  is found to be much larger in magnitude and of opposite sign compared to that of  $A_{1s}$ . This suggests that it cannot be an excited state of the  $A$  exciton as was previously assigned. Using an approximate model, the LGF value of the  $IL$  exciton is shown to be consistent with an interlayer exciton that was earlier identified in few-layer  $2H$ -MoS<sub>2</sub>.

DOI: [10.1103/PhysRevApplied.19.064073](https://doi.org/10.1103/PhysRevApplied.19.064073)

## I. INTRODUCTION

The Landé  $g$  factor (LGF) of excitons in a semiconductor gives a measure of the splitting of the exciton transition energy due to an applied magnetic field  $\mathbf{B}$ . It originates from the Zeeman splitting of energy levels in the conduction and valence bands that are involved in exciton formation. Measuring the LGF can provide information on the origins of the excitons and it is also a property of interest for spintronics [1]. There is currently significant interest in the magneto-optical properties [2] of transition-metal dichalcogenide semiconductors (TMDCs) of the type  $MX_2$  (with  $M = \text{Mo, W}$ ; and  $X = \text{S, Se, Te}$ ) due to novel spin-related phenomena discovered in their electronic band structure, especially in their monolayer and few-layer forms, such as spin-valley coupling and spin-layer locking [3–5], which are relevant for spin-controlled device applications [6].

Giant LGFs have been reported in heterostructures made with two different TMDC materials such as MoSe<sub>2</sub>/WSe<sub>2</sub> [7,8]. Excitons at energies around the direct gaps of both few-layer and bulk TMDCs arise at the  $K$  points of the Brillouin zone and so there is also an interest in studying bulk materials. As such, several types of excitons dominate the optical spectrum of TMDCs even at room temperature due to their large binding energies, and identifying their

origins has been an issue [9]. For instance, in the case of bulk  $2H$ -MoS<sub>2</sub>, one observes a weaker exciton feature just on the higher-energy side of the ground-state  $A_{1s}$  exciton transition. It was earlier thought to be due to the excited state  $A_{2s}$  exciton transition [10]; however, its energy position and magnitude did not agree with the effective-mass Wannier-Mott three-dimensional exciton model when considered together with other observed features [11]. Its energy position also shifted much more with an applied  $\mathbf{B}$  field than  $A_{1s}$ , which cannot be explained if it was  $A_{2s}$  [12]. This feature also survives till high temperatures and gave a wrong estimate of the effective Rydberg constant when considered as  $A_{2s}$  [13]. Thereafter it was suggested that it may originate from a different exciton transition at the  $H$  point of the Brillouin zone [13,14]. However, this idea too had to be discarded since *ab initio* theory calculations suggested that there is a saddle point at the  $H$  point and it cannot sustain an exciton [15].

An interlayer ( $IL$ ) exciton is a state wherein the electron and the hole reside separately on two adjacent layers, as can be expected in heterobilayers [16]. However, such  $IL$  excitons were also shown to exist in homolayer films [17]. In recent studies on bilayer and few-layer  $2H$ -MoS<sub>2</sub>, the weak exciton feature on the high-energy side of  $A_{1s}$  has been attributed to such an  $IL$  exciton [18,19] and it was suggested that this is also what one observes in bulk  $2H$ -MoS<sub>2</sub> [15]. Exciton LGF measurements can throw more light on this issue.

\*sangho10@tifr.res.in

The conventional approach to LGF measurement typically involves measuring milli-electron-volt-range energy shifts of exciton features in a photoluminescence, absorption, or reflectance spectrum under a high magnetic field  $\mathbf{B}$  of several teslas [7,20–24]. It is usually challenging to use such techniques to study microscopic samples such as tiny flakes of TMDC semiconductors [25]. Here we present a circular-polarization-resolved magnetomodulated reflectance (MMR) spectroscopy technique to measure the LGF of excitons using a very small, tens of milliteslas, oscillating  $\mathbf{B}$ . The small-field requirement makes it easy to build a setup around a standard optical cryostat that is compatible with a microscope arrangement for studying small samples. We first describe the technique and the experimental setup. To validate the technique, we use it to measure the LGF of previously studied heavy- and light-hole excitons in a GaAs/Al<sub>0.3</sub>Ga<sub>0.7</sub>As single quantum well (QW) and also determine the limits on LGF estimates. We then use it to study 2H-MoS<sub>2</sub> and show that the  $A_{1s}$  and the next-higher-energy exciton feature have very different LGFs. We analyze the results using an approximate model to understand the LGF values of excitons in bulk 2H-MoS<sub>2</sub>.

## II. WORKING PRINCIPLE

When a magnetic field  $\mathbf{B}$  is applied to a semiconductor, levels in the conduction band (CB) and valence band (VB) that are degenerate in energy but have different total angular momentum projections along  $\mathbf{B}$  undergo Zeeman splitting. For the CB, the splitting energy can be expressed as  $\delta_1 = g_e \mu_B B$ , where  $\mu_B$  is the Bohr magneton. The electron LGF,  $g_e$ , incorporates the net effect of spin, orbital, and valley angular-momentum contributions, the last being relevant in the case of few-layer dichalcogenide semiconductors. A similar expression for the VB levels is  $\delta_2 = g_h \mu_B B$ , with  $g_h$  representing the hole LGF. The transitions between these split CB and VB levels will involve right-circular ( $\sigma+$ ) or left-circular ( $\sigma-$ ) polarized light according to symmetry and angular-momentum-conservation considerations. This general picture of Zeeman splitting is schematically shown in Fig. 1.

Let us consider excitons involving CB and VB levels where the ground-state exciton transition energy in the absence of  $\mathbf{B}$  is  $E_0$ . Then for finite  $\mathbf{B}$  parallel to  $+\hat{z}$ , if  $\sigma+$  light incident along  $-\hat{z}$  causes a transition between split VB and CB states marked “+” in Fig. 1, the transition energy will be

$$E(\sigma+) = E_0 + \frac{1}{2}(g_e - g_h)\mu_B B + \alpha_D B^2, \quad (1)$$

where  $\alpha_D$  is the diamagnetic coefficient [26]. If the direction of  $\mathbf{B}$  is reversed such that  $\mathbf{B}$  is parallel to  $-\hat{z}$ , then relative to it the incident light polarization is now  $\sigma-$  and

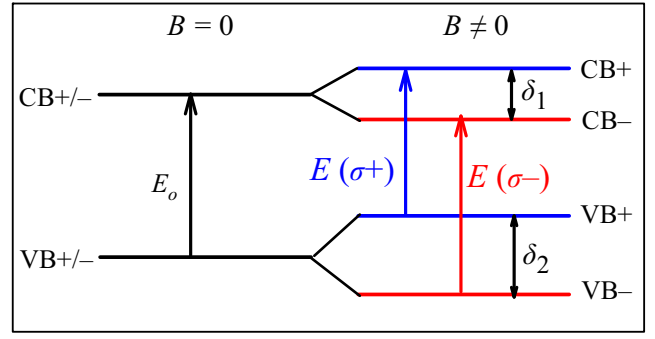


FIG. 1. Schematic representing Zeeman splitting of doubly degenerate conduction-band electron and valence-band hole levels under magnetic field  $\mathbf{B}$ . The + and – signs signify that the levels are connected by transitions involving right ( $\sigma+$ ) and left ( $\sigma-$ ) circularly polarized light.

the transitions will involve the levels marked “–” connected by  $\sigma-$  light. According to Fig. 1 the transition energy now becomes

$$E(\sigma-) = E_0 - \frac{1}{2}(g_e - g_h)\mu_B B + \alpha_D B^2. \quad (2)$$

Thus keeping the incident polarization fixed to, say,  $\sigma+$  and going from  $\mathbf{B} \parallel +\hat{z}$  to  $\mathbf{B} \parallel -\hat{z}$ , the net change in the exciton transition energy will be

$$\Delta E_T = (g_e - g_h)\mu_B B = g_{\text{ex}}\mu_B B, \quad (3)$$

where  $g_{\text{ex}}$  is the exciton LGF. Following the same analysis with  $\sigma-$  polarized incident light will give the same  $|\Delta E_T|$  but with a negative sign.

Usually an exciton transition results in a sharp resonant feature in the reflectance ( $R$ ) spectrum around  $E_0$ . A  $\Delta E_T$  change in the exciton transition energy due to an oscillating  $\mathbf{B}$  would therefore give rise to a periodic change in  $R$  with amplitude  $\Delta R$ , which will be enhanced around  $E_0$ . The  $\Delta R/R$  spectrum represents the magnetomodulated reflectance spectrum. For the case where  $\Delta E_T$  is much smaller than the exciton line broadening, the magnitude of  $\Delta R/R$  will be proportional to  $\Delta E_T$ . The sensitivity of the reflectance of circularly polarized light from a solid in the presence of a magnetic field is essentially the Kerr effect. However, in the usual magneto-optic Kerr effect spectroscopy measurements, which also yield  $\Delta E_T$  [27], a fixed  $\mathbf{B}$  field of large magnitude is used and one measures the difference in the reflectance as the polarization of the incident probe beam is periodically changed between  $\sigma+$  and  $\sigma-$  using standard ellipsometric techniques [28]. Another advantage with MMR is that it is insensitive to any static spurious source of polarization anisotropy since the signal here essentially arises from an oscillating  $\mathbf{B}$  field. However, the oscillating  $\mathbf{B}$  can result in electrical pickups which need to be minimized.

Estimating the LGF of excitons from the circular-polarization-resolved MMR spectrum requires simulation and fitting as follows. We first simulate the  $R$  spectrum. For this we choose the Lorentz oscillator model to represent the exciton's contribution to the dielectric function  $\epsilon(E)$  as a function of photon energy  $E$ , which goes as [29]

$$\epsilon(E) = \epsilon_b + \sum_j \frac{C_j}{E_{0j}^2 - E^2 - i\Gamma_j E}, \quad (4)$$

where  $\epsilon_b = (n_b + ik_b)^2$  is the background dielectric constant. Here  $n_b$  and  $k_b$  ( $\sim 0$ ) are the real and imaginary parts of the background refractive index, respectively; and  $E_{0j}$ ,  $C_j$ , and  $\Gamma_j$  are the exciton transition energy, amplitude factor proportional to the exciton oscillator strength, and broadening parameter of the  $j$ th exciton transition, respectively. The  $E_{0j}$  here includes the local-field correction necessitated by the large density of excitons created in a solid [29].

With the above we obtain the  $R$  spectrum using Fresnel's formula directly or through a transfer-matrix approach in the case of multilayer structures [30]. In the case of a quantum-well sample, Fresnel's formula can still be used by replacing  $C_j$  with  $C_j e^{i\phi}$ , where the phase factor  $\phi$  accounts for interference-induced spectral lineshape changes [31]. Then from matching this calculated  $R$  spectrum with the measured one, we obtain the parameters  $E_{0j}$ ,  $C_j$ ,  $\Gamma_j$ , and  $n_b$ . Thereafter, we simulate the MMR spectrum by calculating

$$\frac{\Delta R}{R} = \frac{\pi}{4} \frac{R(E_{0j} + \Delta E_{Tj}/2) - R(E_{0j} - \Delta E_{Tj}/2)}{2R(E_{0j})}. \quad (5)$$

The values of  $\Delta E_{Tj}$  for which the simulation best fits the measured MMR spectrum gives the Zeeman splitting for the  $j$ th exciton transition, from which we obtain  $g_{\text{ex}}$  using Eq. (3). Thus we need one common  $n_b$  and three parameters per exciton to fit  $R$  and then one more parameter per exciton to fit the MMR spectrum. The above simulation procedure represents a square-wave modulation, unlike the sine-wave modulation in the actual experiment. The factor  $\pi/4$  corrects for the larger amplitude of the first harmonic Fourier component of a square wave. The exciton LGF magnitude and sign are essentially determined by the amplitude and sign of the MMR signal. Noise in the MMR signal is the dominant factor determining the limits on measurable exciton LGF values and the error in it, which will be discussed later. We note that unpolarized magnetomodulation, using a small oscillating  $\mathbf{B}$  riding over a much larger static  $\mathbf{B}$  of several teslas, has been used before [32] but only to identify energy positions of Landau levels created by the static  $\mathbf{B}$  [33].

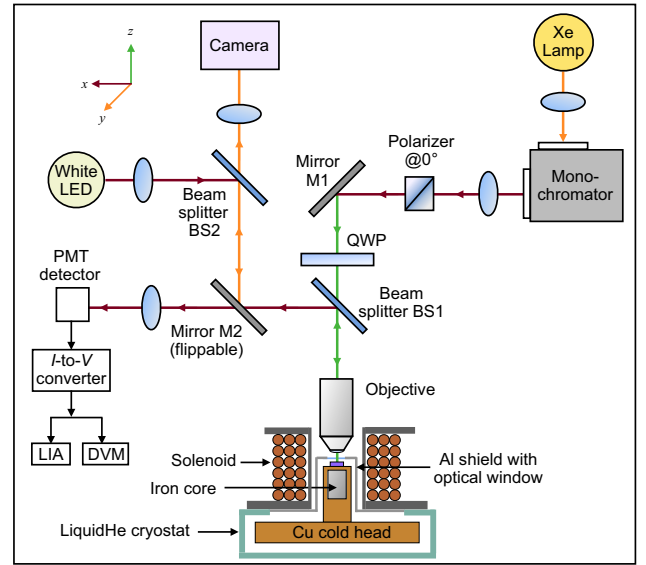


FIG. 2. Schematic of the experimental arrangement for circular-polarization-resolved magnetomodulated reflectance spectroscopy with high spatial resolution. The lock-in amplifier (LIA), dc voltmeter (DVM), and monochromator are interfaced with a computer.

### III. EXPERIMENTAL DETAILS

Figure 2 shows a schematic of the setup for MMR spectroscopy designed to study microscopic samples at cryogenic temperatures. The  $\mathbf{B}$  field is provided by a solenoid coil wound around an Al bobbin with a central hole of 30 mm diameter, to allow for insertion of an objective lens. A continuous-flow He cryostat is used to cool the sample. The cryostat cold finger consists of a protruding Cu cylinder with an aluminum vacuum shield that has an optical window on top. It was designed to fit halfway inside the solenoid. The cryostat along with the magnet were mounted on a  $x$ - $y$  stage, which, along with the camera arrangement, helps in locating the microscopic sample. The objective holder has fine  $z$ -axis control for focusing.

The probe beam is obtained by dispersing light from a 75 W xenon lamp using a monochromator with 0.5 m focal length. Thereafter it is linearly polarized by a polarizer and reflected downwards by mirror M1 towards a broadband quarter-wave plate (QWP) and then onto the objective through a beam splitter (BS1). Mirror M1 does not alter the linear polarization since it reflects along an eigen-polarization axis. The QWP optical axis is rotated to get a  $\sigma^-$  or  $\sigma^+$  polarized probe beam. For BS1 we avoided using common Inconel-coated beam splitters which are ferromagnetic and can give rise to spurious signals; instead, we used Al-coated glass as BS1. Its effect on the circular polarization state after transmission was measured and found to be insignificant. The probe-beam spot size achievable with a  $20\times$  objective was  $13 \times 26 \mu\text{m}^2$ . The reflected light from the sample was detected using a

photomultiplier tube (PMT) and the ac and dc signal components were measured using a lock-in amplifier and dc voltmeter. The mirror M2 on a flip mount is in position initially when the camera arrangement is used for locating a small sample on the substrate and focusing the probe beam onto it and is moved away during measurement.

To increase  $\mathbf{B}$  at the position of the sample, the copper finger has a soft-iron cylinder with low magnetic hysteresis enclosed within, reaching 1 mm below the top. With this arrangement, a maximum sinusoidal current of 3.2 A rms at 160 Hz through the solenoid produced a field of 60 mT rms at the position of the sample near the center of the solenoid coil. This value is after correcting for the influence of the Al vacuum shield. A lower excitation frequency helps reduce inductive heating of the solenoid coil, but too low a frequency increases  $1/f$  noise. Details of field uniformity measurements are given in the supplemental material [34]. To obtain the high oscillatory current, the output from a function generator is passed through a current amplifier circuit [34] with optimal coupling. The MMR signal can ride on an electrical pickup background due to the oscillating  $\mathbf{B}$ ; the background needs to be minimized with appropriate shielding, measured, and then subtracted.

The GaAs/Al<sub>0.3</sub>Ga<sub>0.7</sub>As QW sample used in this study has a single GaAs well of width 4 nm and was grown using metalorganic vapor-phase epitaxy. The MoS<sub>2</sub> sample was a bulk flake with clear surface area less than  $50 \times 50 \mu\text{m}^2$  and  $\sim 7.3 \mu\text{m}$  thick. It was exfoliated from a geological 2H-MoS<sub>2</sub> crystal and then stamped onto a sapphire substrate.

## IV. RESULTS

### A. GaAs/Al<sub>0.3</sub>Ga<sub>0.7</sub>As quantum well

Figure 3(a) shows the  $R$  spectrum of the QW at 6 K, which is an average of the spectrum for  $\sigma-$  and  $\sigma+$  polarizations. It has two strong exciton features around 1.63 and 1.658 eV, arising from transitions between the first confined electron level  $e_{n=1}$  in the CB well and the quantum-confinement-induced split heavy-hole  $hh_{n=1}$  and light-hole  $lh_{n=1}$  levels in the VB well. Here  $n$  is the confinement quantum number. There is also a weak feature around 1.64 eV that originates from the first excited state (the  $2s$  state) of the  $e_1hh_1$  exciton [35], which we have ignored in this analysis. Referring to Fig. 1, CB $\pm$  here corresponds to the  $e_1$  level with atomic  $s$ -orbital character at the  $\Gamma$  point of the Brillouin zone and total angular momentum projection  $m_j = \pm 1/2$  in units of  $\hbar$  along field  $\mathbf{B} \parallel \hat{z}$ . VB $\pm$  corresponds to either the  $hh_1$  or  $lh_1$  levels having atomic  $p$ -orbital character with  $m_j = \pm 3/2$  or  $m_j = \pm 1/2$ , respectively. A transition from VB to CB with  $\Delta n = 0$  is normally allowed. Angular-momentum conservation requires that only  $\sigma+$  ( $\sigma-$ ) polarized light with angular momentum  $-1$  ( $+1$ ) can cause a transition between the

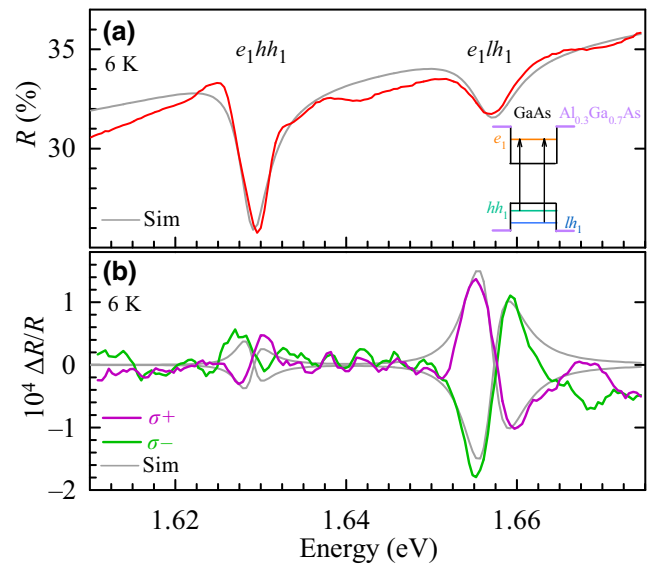


FIG. 3. (a) Reflectance spectrum of a 4-nm-thick GaAs/Al<sub>0.3</sub>Ga<sub>0.7</sub>As QW at low temperature. The inset is a real-space schematic depicting the heavy-hole and light-hole exciton transitions. (b) MMR spectrum for  $\sigma+$  and  $\sigma-$  polarization with  $\mathbf{B} = 45$  mT rms. Simulated spectra are also shown.

$hh_1$  level with  $m_j = +3/2$  ( $-3/2$ ) and the  $e_1$  level with  $m_j = 1/2$  ( $-1/2$ ). Similar polarization selection applies for transitions involving  $e_1$  and  $lh_1$ .

The MMR spectrum of the QW sample shown in Fig. 3(b) was obtained with  $\mathbf{B} = 45$  mT rms. A five-point data smoothing was done to reduce noise. Note that, for the prominent spectral features, the MMR signals for  $\sigma+$  and  $\sigma-$  light have opposite phase as expected from the earlier analysis. For a given polarization, the phase of the signal arising from the  $e_1hh_1$  transition is  $180^\circ$  rotated with respect to that for the  $e_1lh_1$  transition; this indicates that the LGFs for the two transitions have opposite signs. Also, while the strength of the  $e_1hh_1$  transition is much larger than that of  $e_1lh_1$  in the  $R$  spectrum, in the MMR spectrum the latter is much stronger. This indicates that the modulation of the  $e_1lh_1$  transition is larger and therefore it must have a larger LGF magnitude. By matching the simulations with the above measurements, using the steps described earlier, we obtain LGF values  $-0.3 \pm 0.2$  and  $5.9 \pm 0.7$  for the  $e_1hh_1$  and  $e_1lh_1$  exciton transitions, respectively. The exciton LGF in these QWs depends on the well width. For a well width of 4 nm, the expected values [31] of the LGF for  $e_1hh_1$  and  $e_1lh_1$  are around  $-0.5$  and  $6.2$ , respectively.

We next consider the error in the measured LGF values. The MMR signal is essentially an energy derivative signal. The larger the LGF magnitude, the larger will be the Zeeman energy splitting and hence larger the peak MMR signal magnitude. Therefore, noise in the MMR signal directly results in uncertainty in the LGF value and is the

dominant source of error in its measurement here. To estimate this error we can ask: What is the LGF value that will give rise to a peak  $\Delta R/R$  signal that is equal in magnitude to the noise in the measured MMR spectrum? We can find this by using the same simulation procedure as described earlier, with parameters  $n_b$ ,  $C_j$ ,  $E_{0j}$ , and  $\Gamma_j$  obtained from matching the  $R$  and MMR spectra for a particular value of  $\mathbf{B}$ .

For the QW sample, the peak-to-peak noise in the  $\Delta R/R$  signal according to Fig. 3(b) is  $\sim 4 \times 10^{-5}$ . A peak MMR signal of this magnitude corresponds to LGF values  $\pm 0.2$  and  $\pm 0.7$  for  $e_1hh_1$  and  $e_1lh_1$  excitons, respectively, which therefore represents the maximum error in the LGF estimates for these two exciton transitions. Thus our estimated sign and value of the LGF for the QW excitons agree fairly well with previous measurements within error bars, validating this technique. Note that the above LGF values imply very small energy shifts  $\Delta E_T$ ; for example, a maximum of  $21 \mu\text{eV}$  for  $e_1lh_1$  which had a broadening  $\Gamma \sim 7 \text{ meV}$ . This satisfies the requirement  $\Delta E_T \ll \Gamma$  mentioned earlier. It also demonstrates the power of modulation spectroscopy in measuring very small energy shifts [36], which is essentially the reason we are able to measure the LGF with such small  $\mathbf{B}$  fields. The error bars can be minimized by reducing noise through increased averaging.

### B. Bulk $2H$ -MoS<sub>2</sub>

This technique and setup is especially suited for studying microscopic samples such as tiny flakes of TMDCs. Figures 4(a) and 4(b) show the  $R$  and MMR spectra measured on a small flake of  $2H$ -MoS<sub>2</sub> at 6 K, at energies around its lowest direct gap. MMR measurements on  $2H$ -MoS<sub>2</sub> were made for three values of  $\mathbf{B}$ ; the spectrum for  $\mathbf{B} = 60 \text{ mT rms}$  is shown. In the  $R$  spectrum, we see two features, one due to the ground-state  $A_{1s}$  exciton transition and another marked  $IL$ . Note the equally large MMR signal of  $IL$  compared to  $A_{1s}$ , which is quite different from their signal strength in  $R$ . Also their MMR signal for a given  $\sigma-$  or  $\sigma+$  polarization has opposite phase. These two observations already indicate that the LGF of  $IL$  has a larger magnitude and opposite sign relative to  $A_{1s}$ . Following the simulation and matching steps described earlier, we obtain the average LGFs for the  $A_{1s}$  and  $IL$  exciton transitions in  $2H$ -MoS<sub>2</sub> as  $g_{A_{1s}} = -2.5 \pm 0.5$  and  $g_{IL} = 9.7 \pm 2.5$ , respectively. The above  $g_{A_{1s}}$  estimate lies within the range of recently reported values for MoS<sub>2</sub> [23,37,38].

The fact that the  $IL$  feature has a very different LGF in terms of magnitude and sign indicates that it cannot arise from the first excited state  $A_{2s}$  of the  $A$  exciton, as was previously thought [10,11]. A similar feature in the  $R$  spectrum of bilayer, trilayer [18], and bulk [15,17,19,39] TMDCs of  $2H$  configuration has in recent times been identified as arising due to a new kind of exciton named the “interlayer” exciton. It is a state where the electron and

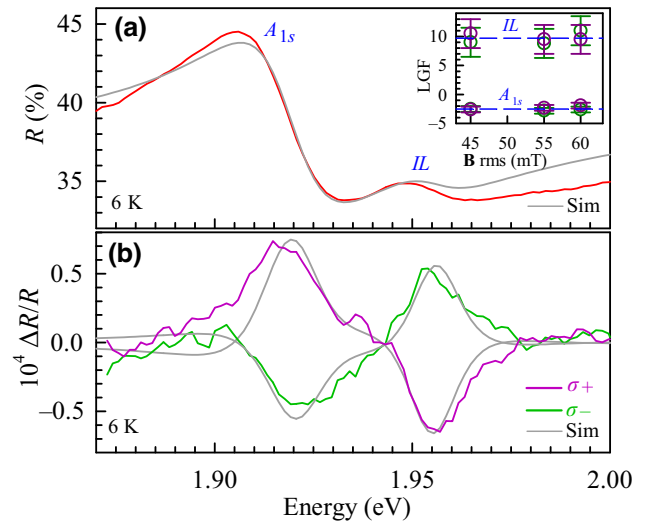


FIG. 4. (a) Reflectance spectrum of bulk  $2H$ -MoS<sub>2</sub> at low temperature. (b) Its MMR spectrum for  $\sigma-$  and  $\sigma+$  polarizations with  $\mathbf{B} = 60 \text{ mT rms}$ . Simulated spectra are also shown. The inset in (a) plots the LGF for the  $A_{1s}$  and  $IL$  excitons obtained for three values of  $\mathbf{B}$ .

the hole reside mostly in adjacent S-Mo-S layers, unlike for  $A_{1s}$ , where they are predominantly in the same layer [15,17].

To understand these results, we discuss the electronic band structure (EBS) of MoS<sub>2</sub>. The  $A_{1s}$  exciton arises due to transitions around the lowest-energy direct gap of bulk  $2H$ -MoS<sub>2</sub> at the  $K$  points of its Brillouin zone. We start with the EBS around the  $K$  points of monolayer MoS<sub>2</sub>, where two adjacent  $K$  points are inequivalent and are labeled  $K+$  and  $K-$  in Fig. 5(a). Here the CB and VB are split into two by spin-orbit coupling and the lower-energy (higher-energy) bands are marked as CB1 (CB2) and VB1 (VB2), respectively. For a monolayer film, only single spin orientation (up or down) can exist at the  $K$  points and their orientation is opposite between CB1 and CB2 or between VB1 and VB2 in the same valley, and also opposite between  $K+$  and  $K-$  valleys [3,4,9].

Figure 5(a) shows MoS<sub>2</sub> as a “darkish” material with VB top and CB bottom having opposite spins, which hampers efficient optical recombination from these levels [40]. In addition, Bloch-wavefunction symmetry considerations determine that, in the  $K+$  ( $K-$ ) valley, VB1 to CB2 transition is possible with  $\sigma+$  ( $\sigma-$ ) polarized light, while VB1 to CB1 transition is forbidden for light polarization in the  $x$ - $y$  plane [3,4,9]. The  $A_{1s}$  exciton transition following such rules is depicted by the vertical arrows in Fig. 5(a). The spin-valley coupling picture is strictly true for monolayers, but weak van der Waals coupling along the  $c$  axis results in such properties being relevant even in multilayer films [5,24,41,42]. Thus, with reference to Fig. 1, the CB+ and VB+ pair here would correspond to CB2 and VB1 levels

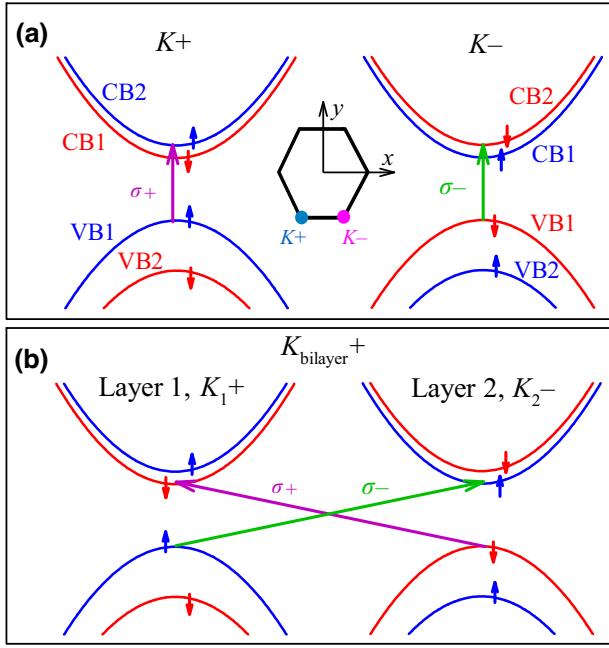


FIG. 5. (a) The CB and VB levels involved in  $A_{1s}$  exciton transition (long vertical arrows) at the  $K+$  and  $K-$  points of the Brillouin zone in monolayer  $\text{MoS}_2$  for  $\sigma+$  and  $\sigma-$  polarizations. The inset shows the Brillouin zone of monolayer  $\text{MoS}_2$ . (b) Similar diagram for an  $IL$  exciton transition (very long tilted arrows) in bilayer  $\text{MoS}_2$  at the effective  $K_{\text{bilayer}+}$  point.

at  $K+$ , and similarly the  $\text{CB}-$  and  $\text{VB}-$  pair correspond to  $\text{CB2}$  and  $\text{VB1}$  levels at  $K-$ .

It has been suggested that, to a first approximation, the individual  $g$ -factor contributions due to spin ( $g_s$ ), orbital ( $g_o$ ), and valley ( $g_v$ ) angular momenta can be added up in the case of few-layer TMDCs [7,21,23,43]. At the  $K$  points, the orbital character at the top of the VB is mostly  $d_{x^2-y^2} \pm id_{xy}$  like [44] with quantum number  $m_j = \pm 2$  and the holes approximately have  $g_o^h \sim \pm 2$  at  $K+$  and  $K-$  valleys, respectively [23]. The bottom of the CB has a dominant  $d_{z^2}$  orbital character [44] with  $m_j = 0$  and thus the electrons approximately have  $g_o^e \sim 0$  at both valleys [23]. There is also a valley angular momentum component in TMDCs with  $g$ -factor contribution  $g_v \sim \pm m_0/m^*$  at  $K+$  and  $K-$  valleys, respectively, where  $m^*/m_0$  is the carrier effective-mass ratio [23,45]. The in-plane electron and hole effective masses at the  $K$  points in bulk  $\text{MoS}_2$  are similar [46], with  $m^*/m_0 \sim 0.5$ ; therefore,  $g_v \sim \pm 2$  at  $K+$  and  $K-$  respectively.

Referring to Fig. 5(a) for the  $A_{1s}$  exciton, we can express the  $g$ -factor contributions at the  $K+$  and  $K-$  valley extrema for  $\sigma+$  and  $\sigma-$  light, respectively, as

$$g_{A_{1s},\sigma+} = g_s^{e,K+} + g_o^{e,K+} + g_v^{e,K+} - \{g_s^{h,K+} + g_o^{h,K+} + g_v^{h,K+}\} \quad (6)$$

and

$$g_{A_{1s},\sigma-} = g_s^{e,K-} + g_o^{e,K-} + g_v^{e,K-} - \{g_s^{h,K-} + g_o^{h,K-} + g_v^{h,K-}\}. \quad (7)$$

Since electron and hole spin orientations are preserved during the transitions and they are in the same valley, the spin and valley  $g$ -factor contributions cancel out in the above expressions. Then with  $g_o^{e,K\pm} = 0$  and  $g_o^{h,K\pm} = \pm 2$  as mentioned previously, we get  $g_{A_{1s},\sigma+} = -2$  and  $g_{A_{1s},\sigma-} = +2$ . Since we are effectively measuring the difference in energy shift between  $\sigma+$  and  $\sigma-$  excitation, we get the net LGF for  $A_{1s}$  to be  $g_{A_{1s}} = g_{A_{1s},\sigma+} - g_{A_{1s},\sigma-} = -4$ . It has been suggested that interlayer interaction in a bulk material tends to bring down the LGF value [20] and therefore our LGF value of  $-2.5 \pm 0.5$  for  $A_{1s}$  is consistent. This estimate is also in fair agreement with reported values of LGF for  $A_{1s}$  in similar bulk or few-layer TMDCs [17,20,22–24,37,38].

Next we consider the  $IL$  exciton transition starting with a bilayer film. There is a  $180^\circ$  in-plane twist of adjacent S-Mo-S layers along the  $\mathbf{c}$  axis in the  $2H$  form of the  $\text{MoS}_2$  crystal structure and also spin orientation is reversed between adjacent layers [5,47]. One may therefore take [17] the effective  $K_{\text{bilayer}+}$  as comprising  $K_1+$  of layer 1 and  $K_2-$  of layer 2 as shown in Fig. 5(b). Calculations based on density functional theory [17] indicate that in this case  $\sigma+$  light can excite an  $IL$  exciton comprising an electron in the  $K_1+$  valley and a hole in the  $K_2-$  valley as shown by a very long tilted arrow in Fig. 5(b). Its  $g$ -factor contribution can then be expressed as

$$g_{IL,\sigma+} = g_s^{e,K_1+} + g_o^{e,K_1+} + g_v^{e,K_1+} - \{g_s^{h,K_2-} + g_o^{h,K_2-} + g_v^{h,K_2-}\}. \quad (8)$$

Also at  $K_{\text{bilayer}+}$ ,  $\sigma-$  light can excite [17] an  $IL$  exciton comprising an electron in the  $K_2-$  valley and a hole in the  $K_1+$  valley, whereby the  $g$ -factor contribution will be

$$g_{IL,\sigma-} = g_s^{e,K_2-} + g_o^{e,K_2-} + g_v^{e,K_2-} - \{g_s^{h,K_1+} + g_o^{h,K_1+} + g_v^{h,K_1+}\}. \quad (9)$$

Since electron and hole spin orientations are preserved in these transitions, the net spin-angular-momentum contribution to  $g_{IL,\sigma+}$  and  $g_{IL,\sigma-}$  will again be zero, and only the orbital and valley angular momenta will contribute. Using previously mentioned numbers, we get  $g_{IL,\sigma+} = +6$  and  $g_{IL,\sigma-} = -6$ , resulting in a net LGF  $g_{IL} = g_{IL,\sigma+} - g_{IL,\sigma-} = 12$ . Similar results can be obtained considering transitions at the  $K_{\text{bilayer}-}$  point. This suggests a much larger value and opposite sign for the LGF of the  $IL$  exciton when compared to the  $A_{1s}$  exciton transition. Our measured value of  $g_{IL} = 9.7 \pm 2.5$  and its sign are consistent

with the above. This is also similar to a suggested value [25] of  $g_{IL} \sim 8$  in bilayer  $2H$ -MoS<sub>2</sub> and a very recent estimate of  $g_{IL} = 9.01 \pm 0.34$  in bilayer MoSe<sub>2</sub> [48]. The  $IL$  exciton transition arises at a higher energy than  $A_{1s}$  most likely because it has a lower binding energy due to the electron and hole being more separated since they are in adjacent S-Mo-S layers, unlike  $A_{1s}$  where they reside in the same S-Mo-S layer [15,17]. We note that, while the above approximate model involving summing up of three individual LGF contributions can broadly explain the measured LGF values in terms of sign and relative magnitudes, to obtain an accurate estimate of the LGF for bulk  $2H$ -MoS<sub>2</sub>, a more rigorous theoretical analysis that also includes effects of electron-hole exchange interactions [9] is necessary.

## V. CONCLUSION

In conclusion, we have demonstrated that circularly polarized magnetomodulated reflectance spectroscopy with very low magnetic fields of the order of tens of milliteslas, can be used to measure the LGF of excitons in semiconductors. The technique requires modeling of the exciton feature in the reflectance spectrum and is therefore suited for cases where a discernible exciton feature exists in the reflectance spectrum. The easy adaptability of this technique for measurement with high spatial resolution enabled studies on microscopic  $2H$ -MoS<sub>2</sub> flakes. There the  $IL$  feature was shown to have an LGF value much larger in magnitude and of opposite sign relative to that for the ground-state  $A_{1s}$  exciton, confirming that it cannot be associated with a pure first-excited-state  $A_{2s}$  exciton. The sign and magnitude of the LGF of the  $IL$  exciton are explainable on the basis of it being an interlayer exciton through an approximate model; however, a proper understanding of its value needs further theoretical investigation.

## ACKNOWLEDGMENTS

The authors acknowledge useful discussions with A. Arora, are grateful for funding support from the Government of India through DAE project No. RTI 4003, and thank S. Sastry for the QW sample.

---

[1] Y. Jiang, M. Ermolaev, G. Kipshidze, S. Moon, M. Ozerov, D. Smirnov, Z. Jiang, and S. Suchalkin, Giant  $g$ -factors and fully spin-polarized states in metamorphic short-period InAsSb/InSb superlattices, *Nat. Commun.* **13**, 5960 (2022).  
 [2] A. Arora, Magneto-optics of layered two-dimensional semiconductors and heterostructures: Progress and prospects, *J. Appl. Phys.* **129**, 120902 (2021).  
 [3] D. Xiao, G. B. Liu, W. Feng, X. Xu, and W. Yao, Coupled Spin and Valley Physics in Monolayers of MoS<sub>2</sub> and Other Group-VI Dichalcogenides, *Phys. Rev. Lett.* **108**, 196802 (2012).

[4] X. Xu, W. Yao, D. Xiao, and T. F. Heinz, Spin and pseudospins in layered transition metal dichalcogenides, *Nat. Phys.* **10**, 343 (2014).  
 [5] A. M. Jones, H. Yu, J. S. Ross, P. Klement, N. J. Ghimire, J. Yan, D. G. Mandrus, W. Yao, and X. Xu, Spin-layer locking effects in optical orientation of exciton spin in bilayer WSe<sub>2</sub>, *Nat. Phys.* **10**, 130 (2014).  
 [6] J. F. Sierra, J. Fabian, R. K. Kawakami, S. Roche, and S. O. Valenzuela, Van der Waals heterostructures for spintronics and opto-spintronics, *Nat. Nanotech.* **16**, 856 (2021).  
 [7] P. Nagler, M. V. Ballottin, A. A. Mitroglu, F. Mooshammer, N. Paradiso, C. Strunk, R. Huber, A. Chernikov, P. C. M. Christianen, C. Schüller, and T. Korn, Giant magnetic splitting inducing near-unity valley polarization in van der Waals heterostructures, *Nat. Commun.* **8**, 1551 (2017).  
 [8] X. Wang, J. Zhu, K. L. Seyler, P. Rivera, H. Zheng, Y. Wang, M. He, T. Taniguchi, K. Watanabe, J. Yan, D. G. Mandrus, D. R. Gamelin, W. Yao, and X. Xu, Moiré trions in MoSe<sub>2</sub>/WSe<sub>2</sub> heterobilayers, *Nat. Nanotech.* **16**, 1208 (2021).  
 [9] G. Wang, A. Chernikov, M. M. Glazov, and T. F. Heinz, Colloquium: Excitons in atomically thin transition metal dichalcogenides, *Rev. Mod. Phys.* **90**, 021001 (2018).  
 [10] A. R. Beal, J. C. Knights, and W. Y. Liang, Transmission spectra of some transition metal dichalcogenides. II. Group VIA: trigonal prismatic coordination, *J. Phys. C: Solid State Phys.* **5**, 3540 (1972).  
 [11] E. Fortin and F. Raga, Excitons in molybdenum disulphide, *Phys. Rev. B* **11**, 905 (1975).  
 [12] M. Tanaka, H. Fukutani, and G. Kuwabara, Excitons in VI B transition metal dichalcogenides, *J. Phys. Soc. Jpn.* **45**, 1899 (1978).  
 [13] N. Saigal, V. Sugunakar, and S. Ghosh, Exciton binding energy in bulk MoS<sub>2</sub>: A reassessment, *Appl. Phys. Lett.* **108**, 132105 (2016).  
 [14] J. Kopaczek, M. P. Polak, P. Scharoch, K. Wu, B. Chen, S. Tongay, and R. Kudrawiec, Direct optical transitions at K- and H-point of Brillouin zone in bulk MoS<sub>2</sub>, MoSe<sub>2</sub>, WS<sub>2</sub>, and WSe<sub>2</sub>, *J. Appl. Phys.* **119**, 235705 (2016).  
 [15] V. Jindal, D. Jana, T. Deilmann, and S. Ghosh, Interlayer and excited-state exciton transitions in bulk  $2H$ -MoS<sub>2</sub>, *Phys. Rev. B* **102**, 235204 (2020).  
 [16] P. Rivera, H. Yu, K. L. Seyler, N. P. Wilson, W. Yao, and X. Xu, Interlayer valley excitons in heterobilayers of transition metal dichalcogenides, *Nat. Nanotech.* **13**, 1004 (2018).  
 [17] A. Arora, M. Druppel, R. Schmidt, T. Deilmann, R. Schneider, M. R. Molas, P. Marauhn, S. M. de Vasconcellos, M. Potemski, M. Rohlfing, and R. Bratschkitsch, Interlayer excitons in a bulk van der Waals semiconductor, *Nat. Commun.* **8**, 639 (2017).  
 [18] I. C. Gerber, E. Courtade, S. Shree, C. Robert, T. Taniguchi, K. Watanabe, A. Balocchi, P. Renucci, D. Lagarde, X. Marie, and B. Urbaszek, Interlayer excitons in bilayer MoS<sub>2</sub> with strong oscillator strength up to room temperature, *Phys. Rev. B* **99**, 035443 (2019).  
 [19] V. Jindal, D. Jana, and S. Ghosh, Electroreflectance spectroscopy of few-layer MoS<sub>2</sub>: Issues related to  $A_{1s}$  exciton subspecies, exciton binding energy, and inter-layer exciton, *J. Appl. Phys.* **132**, 214303 (2022).  
 [20] A. Arora, M. Koperski, A. Slobodeniuk, K. Nogajewski, R. Schmidt, R. Schneider, M. R. Molas, S. M. de

- Vasconcellos, R. Bratschitsch, and M. Potemski, Zeeman spectroscopy of excitons and hybridization of electronic states in few-layer WSe<sub>2</sub>, MoSe<sub>2</sub> and MoTe<sub>2</sub>, *2D Mater.* **6**, 015010 (2019).
- [21] M. Koperski, M. R. Molas, A. Arora, K. Nogajewski, M. Bartos, J. Wyzula, D. Vaclavkova, P. Kossacki, and M. Potemski, Orbital, spin and valley contributions to Zeeman splitting of excitonic resonances in MoSe<sub>2</sub>, WSe<sub>2</sub> and WS<sub>2</sub> monolayers, *2D Mater.* **6**, 015001 (2019).
- [22] Y. Sun, J. Zhang, Z. Ma, C. Chen, J. Han, F. Chen, X. Luo, Y. Sun, and Z. Sheng, The Zeeman splitting of bulk 2H-MoTe<sub>2</sub> single crystal in high magnetic field, *Appl. Phys. Lett.* **110**, 102102 (2017).
- [23] A. V. Stier, K. M. McCreary, B. T. Jonker, J. Kono, and S. A. Crooker, Exciton diamagnetic shifts and valley Zeeman effects in monolayer WS<sub>2</sub> and MoS<sub>2</sub> to 65 Tesla, *Nat. Commun.* **7**, 10643 (2016).
- [24] A. Arora, T. Deilmann, P. Marauhn, M. Druppel, R. Schneider, M. R. Molas, D. Vaclavkova, S. M. de Vasconcellos, M. Rohlfing, M. Potemski, and R. Bratschitsch, Valley-contrasting optics of interlayer excitons in Mo- and W-based bulk transition metal dichalcogenides, *Nanoscale* **10**, 15571 (2018).
- [25] A. O. Slobodeniuk, Ł. Bala, M. Koperski, M. R. Molas, P. Kossacki, K. Nogajewski, M. Bartos, K. Watanabe, T. Taniguchi, C. Faugeras, and M. Potemski, Fine structure of K-excitons in multilayers of transition metal dichalcogenides, *2D Mater.* **6**, 025026 (2019).
- [26] J. van Bree, A. Yu. Silov, P. M. Koenraad, M. E. Flatté, and C. E. Pryor, *g* factors and diamagnetic coefficients of electrons, holes, and excitons in InAs/InP quantum dots, *Phys. Rev. B* **85**, 165323 (2012).
- [27] A. Arora, S. Ghosh, and V. Sugunakar, A mirror based polar magneto-optical Kerr effect spectroscopy arrangement, *Rev. Sci. Instrum.* **82**, 123903 (2011).
- [28] R. M. A. Azzam and N. M. Bashara, *Ellipsometry and Polarized Light* (North-Holland, New York, 1977).
- [29] C. Klingshirn, *Semiconductor Optics* (Springer, Berlin, 2005).
- [30] E. Hecht, *Optics* (Addison-Wesley, Boston, 1998), 3rd ed.
- [31] A. Arora, A. Mandal, S. Chakrabarti, and S. Ghosh, Magneto-optical Kerr effect spectroscopy based study of Landé *g*-factor for holes in GaAs/AlGaAs single quantum wells under low magnetic fields, *J. Appl. Phys.* **113**, 213505 (2013).
- [32] R. L. Aggarwal, in *Semiconduct. Semimetal. Vol. 9*, R. K. Williardson and A. C. Beer eds. (Academic, New York, 1972).
- [33] G. Gatti, M. Iannuzzi, V. Montelatici, R. Bartiromo, E. Borsella, and S. Mobilio, Magneto-reflectance spectra of anisotropic CdS by magnetic field modulation, *Sol. State Comm.* **19**, 823 (1976).
- [34] See Supplemental Material at <http://link.aps.org/supplemental/10.1103/PhysRevApplied.19.064073> for information on bipolar current amplifier circuit, solenoid coil and magnetic field characteristics, and light polarization throughput characteristics.
- [35] A. Mukherjee and S. Ghosh, Origin of additional spectral features in modulated reflectance spectra of 2-dimensional semiconductor systems, *J. Appl. Phys.* **115**, 123503 (2014).
- [36] M. Cardona, *Modulation Spectroscopy*, Solid State Phys. Suppl. 11, F. Seitz, D. Turnbull and E. Ehrenreich eds. (Academic Press, New York, 1969).
- [37] C. Robert, B. Han, P. Kapuscinski, A. Delhomme, C. Faugeras, T. Amand, M. R. Molas, M. Bartos, K. Watanabe, T. Taniguchi, B. Urbaszek, M. Potemski, and X. Marie, Measurement of the spin-forbidden dark excitons in MoS<sub>2</sub> and MoSe<sub>2</sub> monolayers, *Nat. Commun.* **11**, 4037 (2020).
- [38] Y. J. Wu, C. Shen, Q. H. Tan, J. Shi, X. F. Liu, Z. H. Wu, J. Zhang, P. H. Tan, and H. Z. Zheng, Valley Zeeman splitting of monolayer MoS<sub>2</sub> probed by low-field magnetic circular dichroism spectroscopy at room temperature, *Appl. Phys. Lett.* **112**, 153105 (2018).
- [39] J. Horng, T. Stroucken, L. Zhang, E. Y. Paik, H. Deng, and S. W. Koch, Observation of interlayer excitons in MoSe<sub>2</sub> single crystals, *Phys. Rev. B* **97**, 241404R (2018).
- [40] M. R. Molas, C. Faugeras, A. O. Slobodeniuk, K. Nogajewski, M. Bartos, D. M. Basko, and M. Potemski, Brightening of dark excitons in monolayers of semiconducting transition metal dichalcogenides, *2D Mater.* **4**, 021003 (2017).
- [41] J. M. Riley, F. Mazzola, M. Dendzik, M. Michiardi, T. Takayama, L. Bawden, C. Granerød, M. Leandersson, T. Balasubramanian, M. Hoesch, T. K. Kim, H. Takagi, W. Meevasana, P. Hofmann, M. S. Bahramy, J. W. Wells, and P. D. C. King, Direct observation of spin-polarized bulk bands in an inversion-symmetric semiconductor, *Nat. Phys.* **10**, 835 (2014).
- [42] B. Zhu, H. Zeng, J. Dai, Z. Gong, and X. Cui, Anomalously robust valley polarization and valley coherence in bilayer WS<sub>2</sub>, *Proc. Natl. Acad. Sci. U.S.A.* **111**, 11606 (2014).
- [43] D. MacNeill, C. Heikes, K. F. Mak, Z. Anderson, A. Kormányos, V. Zólyomi, J. Park, and D. C. Ralph, Breaking of Valley Degeneracy by Magnetic Field in Monolayer MoSe<sub>2</sub>, *Phys. Rev. Lett.* **114**, 037401 (2015).
- [44] G. B. Liu, W. Y. Shan, Y. Yao, W. Yao, and D. Xiao, Three-band tight-binding model for monolayers of group-VIB transition metal dichalcogenides, *Phys. Rev. B* **88**, 085433 (2013).
- [45] D. Xiao, W. Yao, and Q. Niu, Valley-Contrasting Physics in Graphene: Magnetic Moment and Topological Transport, *Phys. Rev. Lett.* **99**, 236809 (2007).
- [46] H. Peelaers and C. G. Van de Walle, Effects of strain on band structure and effective masses in MoS<sub>2</sub>, *Phys. Rev. B* **86**, 241401(R) (2012).
- [47] Z. Gong, G. B. Liu, H. Yu, D. Xiao, X. Cui, X. Xu, and W. Yao, Magnetoelectric effects and valley-controlled spin quantum gates in transition metal dichalcogenide bilayers, *Nat. Commun.* **4**, 2053 (2013).
- [48] L. Kipcza, A. O. Slobodeniuk, T. Wozniak, M. Bhatnagar, N. Zawadzka, K. Olkowska-Pucko, M. Grzeszczyk, K. Watanabe, T. Taniguchi, A. Babinski, and M. R. Molas, Analogy and dissimilarity of excitons in monolayer and bilayer of MoSe<sub>2</sub>, *2D Mater.* **10**, 025014 (2023).